EXAFS, XANES, and DFT study of the mixed-valence compound YMn_2O_5: Site-selective substitution of Fe for Mn

F. Wunderlich,[1] T. Leisegang,[1] T. Weißbach,[1] M. Zschornak,[1] H. Stöcker,[1] J. Dshemuchadse,[1] A. Lubk,[1] T. Führlich,[1] E. Welter,[2] D. Souptel,[3] S. Gemming,[4] G. Seifert,[5] and D. C. Meyer[1]

[1]*Institut für Strukturphysik, Technische Universität Dresden, 01062 Dresden, Germany*

[2]*Hamburger Synchrotronstrahlungslabor am Deutschen Elektronen-Synchrotron, Notkestrasse 85, 22603 Hamburg, Germany*

[3]*Leibniz-Institut für Festkörper- und Werkstoffforschung Dresden, 01171 Dresden, Germany*

[4]*Institut für Ionenstrahlphysik und Materialforschung, Forschungszentrum Dresden–Rossendorf, 01314 Dresden, Germany*

[5]*Institut für Physikalische Chemie und Elektrochemie, Technische Universität Dresden, 01062 Dresden, Germany*

(Received 24 September 2009; revised manuscript received 3 June 2010; published 12 July 2010)

In YMn_2O_5, the Mn atoms occupy two nonequivalent Wyckoff sites within the unit cell exhibiting different oxygen coordinations, i.e., the system can be characterized as a mixed-valence compound. For the formation of the orthorhombic crystal structure, Jahn-Teller distortions are assumed to play an important role. In this study, we aimed at the investigation of the crystal structure changes upon the substitution of Mn by the non-Jahn-Teller cation Fe^{3+}. Therefore, we synthesized a series of $YMn_{2-x}Fe_xO_5$ powder samples with $x=0$, 0.5, and 1 by a citrate technique. We utilized extended x-ray absorption fine structure (EXAFS) and x-ray absorption near-edge structure (XANES) analysis as well as density-functional theory (DFT) to investigate the two nonequivalent Wyckoff sites within the orthorhombic crystal structure (confirmed for all compositions) occupied by transition-metal atoms. For quantitative determination of structural short-range order, all plausible options of substitution of Fe for Mn are discussed. On the basis of these evaluations, the EXAFS and XANES behavior is analyzed and appropriate crystallographic weights are assigned to the subset of structural models in accordance with the experimental data. From EXAFS analysis, using multiple-scattering theory, we conclude only the 4*h* Wyckoff site to be occupied by Fe [occupancy refined is $(100\pm3)\%$ in case of $x=1$]. Furthermore, taking the XANES spectra into account, we are able to verify the EXAFS results and additionally explain the differences in the Mn *K* XANES spectra in dependence on x to be caused by changes in the dipole transitions to 4*p* final states. From quantitative pre-edge analysis an oxidation number of +4 for the Mn atom for $x=1$ is determined whereas the Fe valence is shown to be unchanged. Since the substitution process only involves one Wyckoff site, the experimentally observed limit to a maximum amount of $x=1$ is explained. Additionally, a possible disorder, discussed in the literature, is not proven for our samples. With DFT calculations, the experimental findings are verified on the basis of the total energy of the different possible electronic configurations. Crystal-field effects are identified to be responsible for the site-selective substitution of Fe for Mn.

DOI: 10.1103/PhysRevB.82.014409 PACS number(s): 75.50.Gg, 61.05.cj, 61.43.Gt

I. INTRODUCTION

During the last decade, extensive scientific research has focused on ferroelectric, ferromagnetic, and ferroelastic materials.[1] Their ferroic properties arise from a spontaneous long-range ordering of, for instance, electric dipoles, magnetic moments, or strained orientational domains. Important characteristics of these materials are, e.g., piezoelectricity or pyroelectricity or giant magnetoresistance. The simultaneous presence of two or more ferroic properties is discussed in terms of multiferroicity.

The fundamental material requirements for the coexistence of multiple ferroic properties have been investigated by various theoretical and experimental approaches.[2–5] As they have to simultaneously meet all criteria specific for each single ferroic property, issues concerning the strength and coupling of the diverse functionalities have been in the very focus of recent studies (see, e.g., the recent collection of review articles in Ref. 6 or Ref. 7).

If these properties are coupled, a large diversity of upcoming applications, e.g., microelectromechanical systems, magnetoelectric transducers, microwave electronics, ferroelectric field-effect transistors as well as data storage and random access memory devices is possible.[1,8–10]

Among these applications, ABO_3 oxides (*A*: alkaline-earth metal and *B*: transition metal) with the perovskite type of structure $CaTiO_3$ [e.g., $BaTiO_3$ (Ref. 11) and $SrTiO_3$ (Ref. 12)], structurally related Ruddlesden-Popper[13] and Aurivillius phases as well as hexagonal manganites with the $LuTiO_3$ type of structure ($RMnO_3$ with *R*: rare earth) and others have great importance due to their comparably straightforward synthesis and controllable diverse properties.[9] Another interesting series of mixed-valence manganites with the $DyMn_2O_5$ type of structure, orthorhombic RMn_2O_5, is in the focus of current research due to the occurrence of antiferromagnetic ordering as well as ferroelectric phase transitions at low temperatures. A significant magnetoferroelectric effect, implying a coupling between ferroelectricity and magnetic ordering, has been observed[7,14–22] and is typical for these substances.[23] This suggests the possibility to control the electric polarization by an external magnetic field giving rise to parts of the above-mentioned applications.

In particular, the compound YMn_2O_5 exhibits a strong magnetoelectric coupling. Since the Y atom has a magnetic moment of zero, the magnetism arises from ordering of Mn magnetic moments only. It is known that the physical prop-

erties of such systems can be influenced by substitution of rare-earth or transition-metal atoms. The magnetic properties of YMn_2O_5, for instance, can be altered by substitution of Y with a magnetic rare-earth atom (RMn_2O_5 with R=Tb, Er, and Ho)[17,24,25] or by substitution of Mn with a different transition metal *TM* [e.g., *TM*=Fe (Ref. 26) and Ga (Ref. 27)]. YMn_2O_5 shows an antiferromagnetic noncollinear ordering of the atomic magnetic moments below a Néel temperature of T_N=45 K.[28] Substituting a part of Mn with Fe ($YMnFeO_5$) results in two antiferromagnetically coupled sublattices.[29] The magnetic moments in each of the sublattices (formal Mn^{4+} and Fe^{3+}) are coupled ferromagnetically. Hence, a global ferrimagnetic structure arises, which was observed below a transition temperature of T_N=165 K.[29] Thus, alloying of Fe enables the materials electric properties to be influenced by an external magnetic field.

Considering the system $YMn_{2-x}Fe_xO_5$, the exact position of Fe atoms within the unit cell is desired to understand and to theoretically model the influence of Fe substitution on the crystal structure and the physical properties (e.g., magnetic ordering). Although chemical considerations suggest that Fe favors the Fe^{3+} state and thus a pyramidal coordination with oxygen, Muñoz *et al.*[29] reported a certain level of Fe/Mn disorder (mixed occupancy of the *TM* Wyckoff sites) within their specimen. From neutron powder diffraction (NPD) data, these authors concluded that about 5% of octahedrally coordinated Fe exists. Also for the compound $YMnGaO_5$ de la Calle *et al.*[27] reported a mixed occupancy of the *TM* sites (3% of Mn 4*f* positions were occupied by Ga and 26% of Ga 4*h* positions were occupied by Mn) using NPD analysis.

The composition of the YMn_2O_5 compound suggests formally multivalent Mn ions ($YMn^{4+}Mn^{3+}O_5$) with partially filled *d* shells. Electrons occupying these *d* shells can be energetically degenerate within a high site-symmetric atomic environment. Due to crystal-field effects, a deformation of this atomic environment to lower symmetry can occur which removes this degeneracy. In this case, the ion becomes a Jahn-Teller ion.[30,31] In comparison to Mn^{3+}, Mn^{4+}, and Fe^{4+} Jahn-Teller capable ions, the Fe atom favors a Fe^{3+} oxidation state with a high-spin $3d^5$ electronic configuration, which is not a Jahn-Teller ion.[30,31] Now the question arises if Jahn-Teller effects influence the substitution behavior of Fe for Mn. To answer this question, the exact Wyckoff site occupied by Fe atoms within the crystal structure of YMn_2O_5 has to be evaluated including possible disorder therein. Therefore, we have investigated a composition series of isostructural $YMn_{2-x}Fe_xO_5$ compounds with x=0, 0.5, and 1 using element-sensitive transmission extended x-ray absorption fine structure (EXAFS) and x-ray absorption near-edge structure (XANES) analysis in combination with quantum theoretical calculations within the framework of density-functional theory (DFT). The electronic configuration of the *TM* ions with respect to their local environment will be studied.

Crystal structure

The RMn_2O_5 (R=Y, La, Pr, Nd, Sm-Er, Yb, Lu, and Bi) compounds crystallize in the $DyMn_2O_5$ structure type with

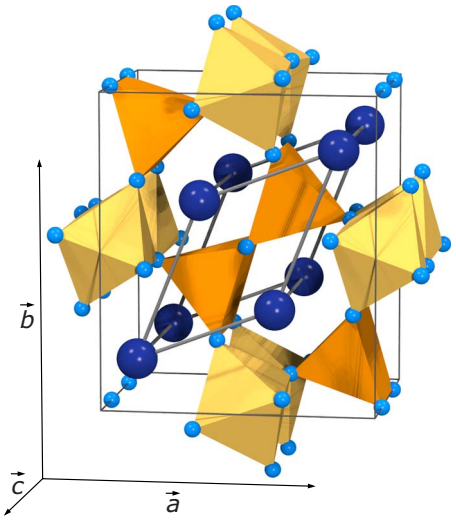

FIG. 1. (Color online) Sketch of the orthorhombic structure of $YFeMnO_5$ with space-group symmetry *Pbam* (55) [a=7.2674 Å, b=8.4760 Å, and c=5.6692 Å at ambient conditions (Ref. 32)]. The unit cell (thin gray lines), yttrium (large spheres), oxygen (small spheres), and both transition-metal sites, TM_O (on 4*f*) centered within the octahedra and TM_P (on 4*h*) within the pyramids, are drawn. The structure can be described by a net of edge-sharing octahedra as well as tetrahedra stacked along the *c* direction, which both are corner-linked.

primitive orthorhombic space-group symmetry *Pbam* (55) and four formula units per unit cell. Alloying of Fe conserves the space-group symmetry.[32] For the isostructural $YMn_{2-x}Fe_xO_5$ compounds, no structural phase transition or nonlinear behavior of structural parameters is observed in the range of x=0–1 at ambient conditions.[32]

It is common for oxides to characterize the structure in terms of polyhedra formed by the oxygen environment of the *TM* atoms. For the *TM* atoms, two distinct Wyckoff sites (4*f* and 4*h*) exist in the unit cell: 4*f* (TM_O) with octahedral and 4*h* (TM_P) with pyramidal coordination with oxygen and formal oxidation state of +4 and +3, respectively. While the octahedra form edge-sharing chains along the crystallographic *c* axis, the tetragonal pyramids form units of two, connecting chains of octahedra by corners (see Fig. 1). The Y atoms are coordinated by oxygen atoms of both these polyhedra forming distorted scalenohedra. In Table I, the occupied Wyckoff sites, site symmetries, and fractional coordinates are summarized.

II. METHODS

A. Sample preparation

Polycrystalline $YMn_{2-x}Fe_xO_5$ samples with x=0–1 have been prepared by a modified citrate technique.[33] The precursor materials were obtained by dissolving the starting material, the rare-earth oxides, Fe-oxalate and $MnCO_3$, in dilute HNO_3 (1:8) and citric acid (1:2). As-prepared precursors were mixed in an appropriate ratio and citric acid (1:4) was added for further polymerization. The mixture was dried at a temperature of 180 °C for a duration of about 10 h where

TABLE I. Wyckoff sites, site symmetries, and fractional coordinates of the orthorhombic YMn_2O_5 structure with space-group symmetry *Pbam* (55) are listed. The atoms are labeled for clarity and are referred to in the text.

Atom	Label	Wyckoff site	Site symmetry	x/a	y/b	z/c
Y	Y	4*g*	..*m*	x_Y	y_Y	0
Mn/Fe	TM_O	4*f*	..2	0	1/2	z_{TM_O}
Mn/Fe	TM_P	4*h*	..*m*	x_{TM_P}	y_{TM_P}	1/2
O	O1	4*e*	..2	0	0	z_{O1}
O	O2	4*g*	..*m*	x_{O2}	y_{O2}	0
O	O3	4*h*	..*m*	x_{O3}	y_{O3}	1/2
O	O4	8*i*	1	x_{O4}	y_{O4}	z_{O4}

polymerization and partial decomposition of the organic components occur. The obtained porous x-ray amorphous gel was heated to a temperature of 600 °C in air to remove all the nitrates and organic traces so that a fine powder could be precipitated. The final product was synthesized at a temperature of 900 °C and 200 bar of oxygen pressure for a duration of 12 h to hold the valence of the Mn^{4+} cations and to increase the reaction rate of the precursors. Polycrystalline powders obtained that way, with grain size of about 50 nm, were subjected to scanning electron microscopy and x-ray powder-diffraction analysis exhibiting a highly crystalline main phase and a small amount of additional phases with compositions Fe_2O_3 and Y_2O_3 in case of $x=0.5$ and 1 (in total less than 0.3 wt. % and 8.1 wt. %, respectively).[32] These powders were used for EXAFS experiments. They were carefully mixed with cellulose powder in a desired ratio and pressed to pills. The amount of powder material (approximately 64 mg and 14 mg for experiments at Y *K* and Mn *K*/Fe *K* absorption edges, respectively) was calculated in advance to yield a product $\mu \cdot d$ of 1.5 (μ: absorption coefficient, *d*: sample thickness) for every absorption edge using the program XAFSMASS (Ref. 34) taking also the absorption edge energy into account. Finally, six samples (two samples for each composition: one for investigating the vicinity of the Y *K* and one for investigating the vicinity of the Mn *K*/Fe *K* absorption edge, respectively) were prepared for the experiments.

B. Extended x-ray absorption fine structure

The term EXAFS refers to energy-dependent oscillations of the x-ray absorption coefficient on the high-energy side of an absorption edge—the whole data set is denoted as x-ray absorption spectroscopy (XAS) data. The difference between the measured absorption coefficient and the theoretical coefficient calculated for isolated atoms is attributed to interference of the outgoing part of the wave function of an emitted electron and the part backscattered from the neighboring atoms. Using this method, the short-range order around resonantly excited atoms can be evaluated and sorts as well as positions of the neighboring atoms can be determined. Details of EXAFS theory can be found in, e.g., Lee *et al.*[35] For single-scattering theory, the EXAFS function $\chi(k)$ (Ref. 36) can be written as

$$\chi(k) = \sum_{j=1}^{N} \frac{n_j}{k \cdot r_j^2} \cdot D_j(k, r_j) \cdot F_j(k) \cdot e^{(-\sigma^2 k^2)} \sin(2kr_j + \phi_j) \tag{1}$$

with *N* being the number of nonsymmetry-equivalent electron-scattering paths, n_j the multiplicity of scattering path *j*, r_j half their length, *k* the wave number of the electron wave, $D_j(k, r_j)$ a factor accounting for inelastic losses, $F_j(k)$ the backscattering amplitude, σ^2 which can be interpreted in terms of a Debye-Waller factor, and ϕ_j being the phase shift of the electron wave at the absorber and at the backscattering atom. In our discussion section we will refer to Eq. (1).

Structural information from the EXAFS spectra is obtained by fitting the $\chi(k)$ spectrum with a sum of photoelectron scattering paths using a proper starting model. The photoelectron scattering path can be either a single-scattering path, which corresponds to the direct scattering by the neighboring shell or a multiple-scattering path, which includes multiple scattering by more than one neighbor.

The EXAFS measurements were performed at beamline C (CEMO) (Ref. 37) of the Hamburger Synchrotronstrahlungslabor (HASYLAB) at Deutsches Elektronen-Synchrotron (DESY) in transmission mode at a vacuum pressure of $p < 10^{-5}$ mbar at room temperature, where oxygen losses can be neglected. For selection of primary beam photon energy, a fixed-exit Si (111) double crystal monochromator[38] was employed. The energy was calibrated using different metallic foils. Primary and transmitted intensities were recorded using two independent gas ionization chambers filled with a dedicated gas mixture [calculated with the program XAFSMASS (Ref. 34)]. The EXAFS spectra were collected at the Y *K*, Mn *K*, and Fe *K* absorption edges using optimized scan parameters of the beamline software. An energy range of the exciting photons of $E=16\,788-18\,038$ eV, $E=6400-7400$ eV, and $E=6862-8112$ eV (Y *K*, Mn *K*, and Fe *K* absorption edge) and an energy step width of $\Delta E \leq 10$ eV before, $\Delta E = 0.5$ eV in the vicinity and $\Delta E = 0.5-2.5$ eV above the absorption edge were applied. The respective energy step width above the absorption edge was calculated to ensure an equidistant step width in *k* space of $\Delta k = 0.02$ Å^{-1} for the EXAFS region of the spectra. Exemplarily, in Fig. 2 the raw data of the Y *K* as well as Mn *K* and Fe *K* XAS are shown.

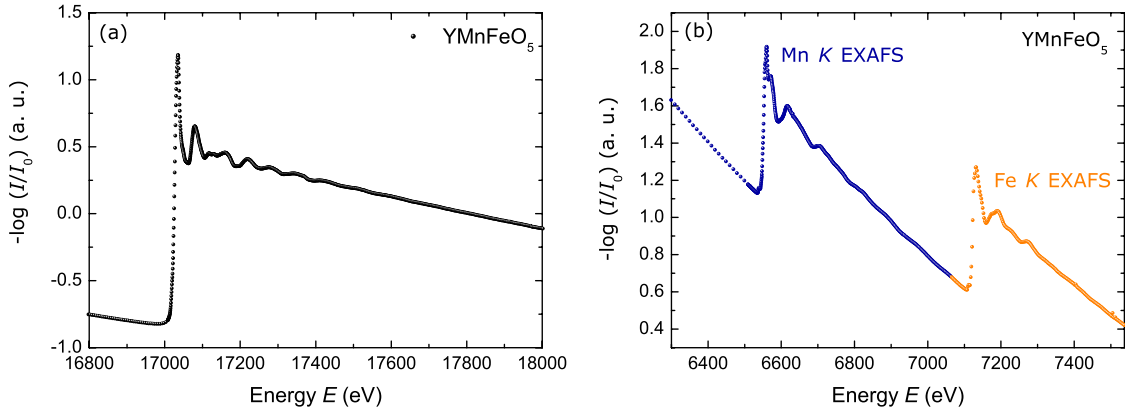

FIG. 2. (Color online) Raw XAS data of the Y K (a) as well as Mn K and Fe K (b) absorption edges of the $YMnFeO_5$ sample collected in transmission mode (I_0: primary beam intensity, I: transmitted intensity). From (b) can be seen that for the Mn K EXAFS only a limited energy range of about 570 eV above the absorption edge can be used for the quantitative analysis.

Prior to the quantitative analysis a data reduction in the EXAFS spectra was performed using the ATHENA software.[39] In this respect, the spectra were normalized to an edge jump of 1 and the absorption coefficient of the isolated atoms $\mu_0(E)$ was extracted by fitting a cubic spline function to the data. After subtraction of the atomic background, the conversion from E to k scale was performed. The quantitative analysis, i.e., refinement, of the EXAFS data was done using the program ARTEMIS (Ref. 39) based on the FEFF 6 code.[36] Structure parameters for the starting models were taken from Ref. 32, which have been obtained by x-ray powder-diffraction analysis of the same samples. Individual clusters of atoms were then generated from the $YMn_{2-x}Fe_xO_5$ unit cell using the ATOMS program of the ARTEMIS software package[39] and taking the different sites for the core atoms into account. The distribution of Mn and Fe in the unit cell was determined by fitting a linear combination of the plausible models to the data; the sum of the coefficients was restrained to unity. For fitting the Fe/Mn EXAFS in k space as well as r space (r: radius) a k range of $k=2-14$ Å^{-1} for the Fe EXAFS and of $k=2-12$ Å^{-1} for the Mn EXAFS, respectively, and a $\Delta k'=1$ Å^{-1} as well as $\Delta r'=0.2$ Å (parameters according to Hanning, Parzen, and Kaiser-Bessel window functions,[39] where both parameters and type of window functions have negligible effects on the fit results) and an r range of $r=1-6$ Å for all samples was used. The limited k range in case of the Mn EXAFS is attributed to the appearing Fe K absorption edge and thus to a limited energy range of 570 eV [see Fig. 2(b)].

In order to fit the final structure models, six free parameters were used: one for taking inelastic losses into account (S_0^2), three displacement parameters σ_Y^2, σ_{TM}^2, and σ_O^2, a parameter related to valence states, core relaxations and other complex effects occurring near the absorption edge energy[35] and a parameter δ characterizing the distribution of Mn and Fe. The parameter δ will be described in more detail in Sec. III B. No parameter for path-length corrections Δr was taken into account since no improvement of the fit quality could be achieved. These parameters seemed to be the best compromise between small quality parameters (R values) and a limited number of refined parameters yielding the largest data-to-parameter ratio and small confidence intervals.

C. X-ray absorption near-edge structure

XANES spectra were extracted from the XAS data. The absorption edge energies were determined by calculating the first derivative of the XAS data and fitting the first maximum by a Gaussian profile (the error of such a fit was taken as the error for the absolute value of the center of the profile). Theoretical curves were calculated for clusters of 7 Å radius with the absorbing atom situated in the middle using FEFF 8.2 (Ref. 40) in XANES mode. Here, the scattering potential for the cluster is calculated self-consistently from first principles and a real-space multiple-scattering approach based on muffin-tin potentials is employed. Orbital basis functions up to $l=3$ (Y, Mn, and Fe) and $l=2$ (O) were applied. The core hole of the absorbing atom was included and the exchange and correlation function given by Hedin and Lundqvist[41] was applied. Scattering of x rays by the cluster was then simulated using a real-space Green's-function method,[42] which results in the calculation of the energy-dependent absorption coefficient $\mu(E)$. As stated before, structure data from Ref. 32 were used in the calculation of the cluster geometry with the program ATOMS from the ARTEMIS package.[39] Unlike in a standard FEFF calculation, the crystallographically different sites of the same element were treated independently to exploit the different charges at the Mn sites. Polarization effects on the data were not accounted for since the measurements were carried out on powder samples with crystallites of random orientation. We did not consider atomic displacements in terms of a Debye-Waller factor since these effects are small in the absorption near-edge region.[43]

D. Density-functional theory

DFT band-structure calculations with the all-electron full-potential local orbitals code FPLO (Ref. 44) were employed to calculate total energies and electron densities of states with the exchange and correlation potential by Perdew and Wang[45] in a scalar-relativistic formalism. The structural unit cell studied here comprises 32 atoms and contains three dif-

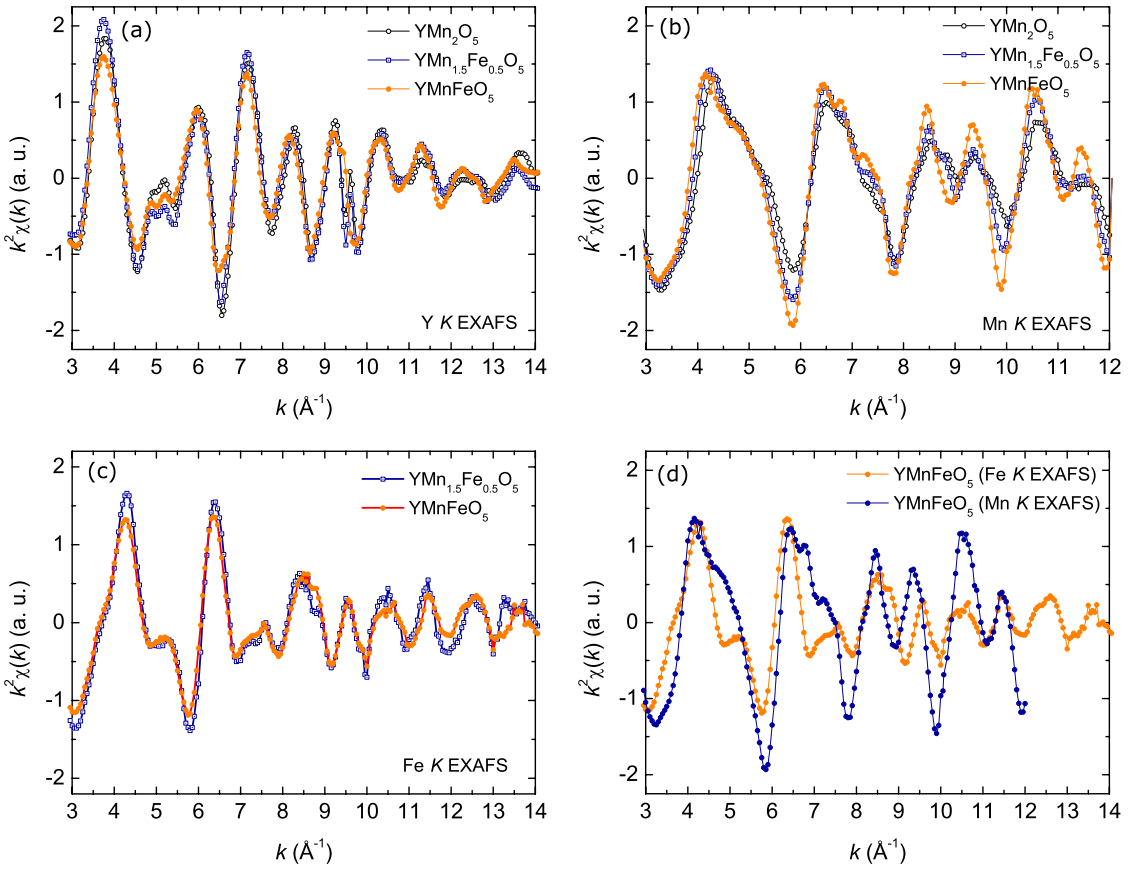

FIG. 3. (Color online) Extracted experimental EXAFS functions $\chi(k)$ of the investigated samples weighted by k^2 are shown for (a) the Y K, (b) the Mn K, and (c) the Fe K absorption edge. In (b) a systematic variation in the curves with composition x can be seen. In (d) a comparison of the Fe K and Mn K EXAFS function for the $YMnFeO_5$ sample is shown, indicating that no statistical distribution (see text) of Mn and Fe over both Mn sites (TM_O, TM_P) exists.

ferent metal coordination polyhedra in up to four different spatial orientations. The structure data were taken from Ref. 29 consistent with the data of Ref. 32. The magnetic unit cell, not studied here, is at least twice as large as the structural one, hence one may assume that the structural unit cell is dominated by crystal-field effects. To investigate this assumption, on-site effects such as atom size and crystal field in the different coordination polyhedra were separated computationally from the more complex intersite magnetic coupling between the different transition-metal sites in adjacent polyhedra. For this purpose the band-structure calculations were augmented by an analysis based on cluster models. Such calculations, performed in large supercells with otherwise identical numerical settings, allow a site-, symmetry-, charge-, and element-resolved analysis of the crystal-field interactions and local magnetic moments without the need for treating the more complex magnetic interactions. They are very helpful for the interpretation of the complex results of band-structure calculations and give an insight into the electronic structure from a local—more chemical—point of view.

III. RESULTS

A. EXAFS data

We want to start with the results of the experimental findings. High-quality EXAFS data were collected for all samples. Figure 3 summarizes the extracted EXAFS functions $\chi(k)$, weighted with the square of the wave number k^2, of all samples and absorption edges. For the Y K EXAFS function [Fig. 3(a)] no systematic variation in the data with respect to the Fe content x can be seen. Nevertheless, small differences in the low-k regions occur. In Ref. 32 it was reported that the Y-O scalenohedra get more and more distorted with growing x. This results in a greater variance of Y-O distances. So it was expected that the Y K EXAFS for $x=1$ exhibits a higher damping of the oscillation amplitudes compared to the other samples, i.e., the sample with $x=0$. Indeed, this trend is discernible in Fig. 3(a). Concluding, the Y K EXAFS data are not appropriate for elucidating the position of Fe within the unit cell. In Fig. 3(b) all three Mn K EXAFS functions are shown. Here significant and systematic differences can be seen. The signal enhances with x (a decrease in oscillation damping from $x=0$ to $x=1$) as was expected from a decreasing distortion of the TM_P-O and TM_O-O polyhedra.[32] Therefore, we can assume that these spectra are appropriate for Fe localization. Regarding the Fe K EXAFS functions in Fig. 3(c), only minor differences in the high-k region can be found. Fourier analysis of this region shows that the differences can be attributed to path lengths of 3–4 Å. Since there are only small differences between the two EXAFS functions, one can already assume that Fe is located at the same site for both samples. Figure

TABLE II. Experimental absorption edge energies of the investigated samples are listed (note that for $x=0$, there are no Fe atoms and thus no XANES spectrum was recorded). Whereas for the Y K and Fe K absorption edge energies a decreasing trend is observed, the differences are rather small. However, the Mn K absorption edge energies show a significant systematic increase with increasing Fe content x.

x	E(Y K) (eV)	E(Fe K) (eV)	E(Mn K) (eV)
0	17026.91(9)		6552.93(18)
0.5	17026.89(8)	7126.23(11)	6553.91(20)
1	17026.62(7)	7125.72(14)	6554.49(22)

3(d) illustrates the difference between Fe K and Mn K EXAFS showing that there are significant differences between the local structure of Fe and Mn atoms. We will refer to this aspect in Sec. IV A.

B. XANES data

High-quality XANES spectra were obtained for all atomic species. Comparing all spectra, in particular, the absorption edge energies, rather small differences within 2σ (σ: error) were found for the Y K and Fe K XANES as can be seen from Table II and Fig. 4(b). Nevertheless, for their edge energies (E) a decreasing trend with increasing Fe content is observed: $\Delta E=0.3(2)$ eV for the Y K and $\Delta E=0.5(3)$ eV for the Fe K edge energy. In case of the Mn K XANES [see Fig. 4(a)], a shift of the absorption edge energy to higher values can be seen with increasing Fe content x. This shift amounts to $\Delta E=1.56(40)$ eV between the Mn K edge energies of compositions $x=1$ and $x=0$.

C. DFT calculations

Spin-polarized band-structure calculations of the full structural unit cell yield a preference for Fe at the pyramidal site which amounts to 0.2 eV per Fe atom for the experimental structure $YFeMnO_5$ (Ref. 32) and to 0.3 eV after DFT optimization. As the pyramid exhibits longer TM-O distances than the octahedron this finding may reflect that the ionic radius of fivefold coordinated Fe^{3+} (0.58 Å) is slightly larger than that of fivefold coordinated Mn^{3+} as well as sixfold coordinated Fe^{4+} and Mn^{4+} (all about 0.55 Å).

In accordance with the experimental structures of YMn_2O_5 and $YMnFeO_5$ (Ref. 32), however, DFT calculations find Mn^{3+} located closer to the basal plane of the pyramid whereas Fe^{3+} is shifted toward the oxygen atom at the top of the pyramid (apex atom) by 0.2 Å relative to the Mn position. Thus, despite being formally the largest ion, Fe^{3+} forms the shortest metal-oxygen bond within the crystal. These results imply that more detailed electronic-structure data of the ions and their immediate surrounding are required to analyze structures as complex as that of $YFeMnO_5$.

To address the above conclusions a cluster-based analysis of the local interactions was carried out with the coordination polyhedra of the full experimental structure as smallest model clusters. Assuming formal ionic charges for all ions in the TM-O polyhedra, i.e., TM^{3+}, TM^{4+}, and O^{2-}, the resulting cluster models are $TMO_5^{6-/7-}$ for the pyramidal site and $TMO_6^{8-/9-}$ for the octahedral one. The embedding crystal potential, which compensates those charges in the extended crystal, is accounted for by applying a fixed charge to the cluster. The oxygen positions were kept fixed and the position of the TM atom was varied along the high-symmetry line, which connects TM and apex atom of the pyramid or TM and one of the apex atoms of the octahedron, to find the total-energy minimum (see Table III). For the octahedron, the displacement of the TM ion toward an apex oxygen atom is unfavorable for all TM ions. In contrast, the TM position within the pyramid is sensitive to the formal charge and the type of the ion.

The displacements away from the experimentally observed position (in $YMnFeO_5$) of the TM in the pyramid are largest for the principally Jahn-Teller active ions Fe^{4+} and Mn^{3+} whereas the Mn^{3+} relaxes toward its experimentally observed position in YMn_2O_5. Hence, the present cluster cal-

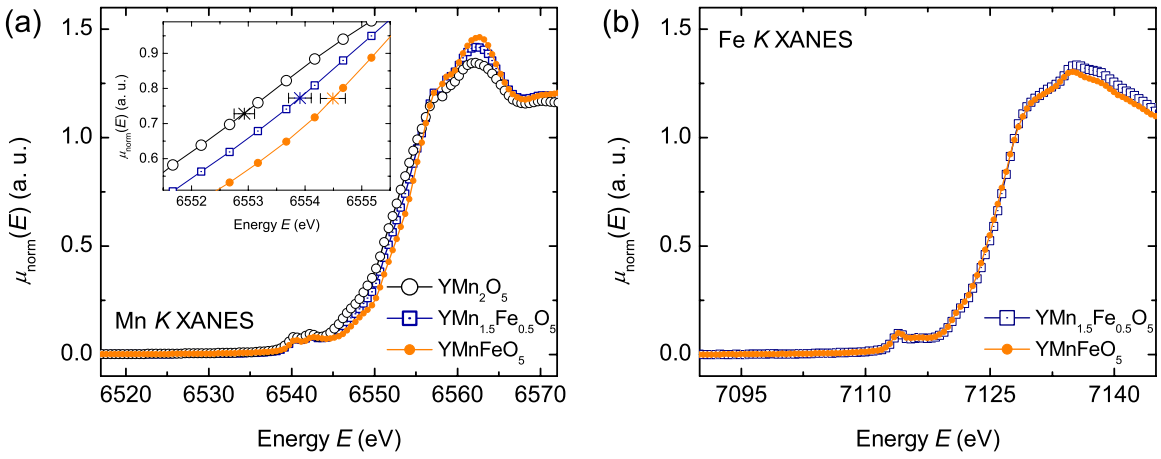

FIG. 4. (Color online) Experimental XANES spectra at (a) the Mn K and (b) the Fe K absorption edge of all investigated samples are depicted. The Mn K edge inflection points are marked by " $*$ " in the inset in (a) (error bars are indicated), which shows a magnified region of the spectra. A systematic increase in E(Mn K) with x is observed whereas for the Fe K XANES no changes can be seen.

TABLE III. Spin states and restricted geometry for several charged TMO_5 (oxidation state: −7/−6) and TMO_6 (oxidation state: −9/−8) clusters. For the spin state, the number of unpaired electrons is written in parentheses. It corresponds to the spin-density difference of the whole cluster. The distance d is calculated from the TM ion position given in the structure data (Ref. 32). The direction of possible displacements is restricted as discussed in the text. A positive value means a shift toward the apex oxygen. DFT total energies for all electrons are given.

TM ion	Spin state (unpaired electrons)	d (Å)	All electron total energy (keV)
Octahedron:			
Fe^{3+}	high (5)	0	−46.60
Fe^{4+}	low (2)	0	−46.64
Mn^{3+}	high (4)	0	−43.49
Mn^{4+}	high (3)	0	−43.54
Pyramid:			
Fe^{3+}	high (5)	−0.01	−44.64
Fe^{4+}	high (4)	−0.05	−44.67
Mn^{3+}	high (4)	−0.13	−41.54
Mn^{4+}	high (3)	+0.01	−41.57

culations reproduce the variation in this position between the $x=0$ and $x=1$ compounds, although the coordinates of the oxygen atoms of the pyramid are fixed at the values of the $x=1$ compound.

As only one TM site is present in each of the model clusters, the magnetic moments were directly obtained from the spin-density differences (see Table III), and the preferred spin configurations were investigated by setting the total spin polarization as boundary condition. In general, the high-spin states are lower in energy by 0.2 eV than the low-spin configurations except for the Fe^{4+} ion within the octahedron.

Furthermore, total-energy differences allow to deduce (i) which formal oxidation states occur at the two sites and (ii) which atom prefers which site. To answer the first question, the energy differences ΔE were evaluated, which compare the two combinations (TM_O^{4+}/TM_P^{3+}) and (TM_O^{3+}/TM_P^{4+}),

$$\Delta E = [E(TM_O^{3+}) + E(TM_P^{4+})] - [E(TM_O^{4+}) + E(TM_P^{3+})]. \quad (2)$$

The differences obtained are $\Delta E=11.2$ eV for Mn at the pyramid position and $\Delta E=12.4$ eV for Fe at the pyramid position. These results support the Madelung argument that the higher coordinated TM ion in the octahedron exhibits a higher formal oxidation state than the less coordinated site within the pyramid. The large energy difference indicates that the ion combinations with the reversed oxidation states (TM_O^{3+} and TM_P^{4+}) can be neglected. Then, the second question can be answered by calculating the energy difference

$$\Delta E = [E(Fe_O^{4+}) + E(Mn_P^{3+})] - [E(Mn_O^{4+}) + E(Fe_P^{3+})], \quad (3)$$

which is 1.0 eV in favor of Fe^{3+} within the pyramid.

IV. DISCUSSION

A. Preliminary considerations

Before we start to analyze our experimental data quantitatively, we want to do some preliminary considerations. In the following, we will discuss the possible situations for probable substitution positions of Fe in $YMn_{2-x}Fe_xO_5$ and, in particular, the influence of the chosen site for Fe on the EXAFS spectra. Let us first consider the following three simple alternative assumptions for the distribution of Mn and Fe in the unit cell: (A) Fe and Mn are distributed statistically to an equal amount (and homogeneously across the sample) on both Wyckoff sites TM_O and TM_P. (B) Fe is located completely on position TM_O and Mn on TM_P. (C) Fe is located completely on position TM_P and Mn on TM_O.

For the quantitative examination, a more general model will be used at the end: (D) Fe is distributed inhomogeneously over both Wyckoff sites (including antisite disorder).

Furthermore, let us consider the theoretical backscattering amplitudes of the atoms, the phase shifts of the emitted photoelectron waves for those elements acting as absorbers of x rays (emitters of photoelectron waves) as well as the phase shifts of the photoelectron waves for those elements acting as backscatterers.[46] The comparison of these theoretical data yields the following important aspects for the interpretation of the EXAFS spectra: (i) Mn and Fe backscattering amplitudes as well as the phase shifts are almost identical and (ii) the influence of Y and O can be well separated in the EXAFS spectra. Hence, in case of Y as absorbing atom, one cannot distinguish between Fe and Mn, independent of which is acting as backscattering atom in a scattering path. Additionally, the same holds for Fe being the absorbing and Mn the scattering atom and vice versa. This explains why the Y K EXAFS spectra do only slightly differ, presumably due to different atomic distances. Nevertheless, it remains possible to distinguish between Fe on TM_O or TM_P site since the particular sites have a significantly different atomic environment. It is worth to point out that due to this fact one can use the EXAFS measurement to supplement a standard x-ray diffraction experiment (that cannot resolve which site is occupied by which TM). As expected, the contributions of Y and O atoms as well as Fe/Mn to the EXAFS signal can be well separated.[46]

Let us now consider the possible situations for the distribution of Fe on both TM sites existing in $YMnFeO_5$ in a simplified and rather schematic manner. [For quantitative analysis we used the real cluster models generated from the unit cell of $YMn_{2-x}Fe_xO_5$ (Ref. 32)]. Due to the electronic structure of Mn/Fe only the situations depicted in Fig. 5 are taken into account. In (a)–(c) the situations for Mn as absorbing atom and in (d)–(f) those for the Fe atom are shown. In accordance with Eq. (1) the EXAFS signal can be described by superposition of subsignals. The exact coefficients that weight the individual subsignals (a), (b), and (c) as well as (d), (e), and (f), respectively, can be derived by combinatorial considerations. Based on the assumption that the occupation of the TM_P site does not depend on the occupation of the TM_O site, all probabilities to find the above cases (a)–(f) can be expressed by a product of two independent probabili-

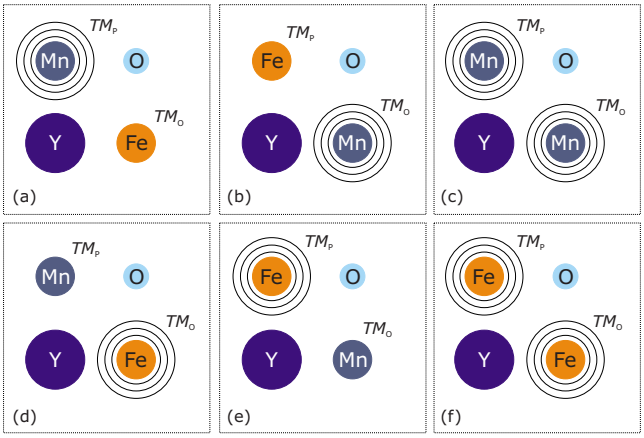

FIG. 5. (Color online) Schematic and simplified representation of the situations possibly realized in $YMn_{2-x}Fe_xO_5$. The situations that create the Mn EXAFS signal and the Fe EXAFS signal are shown in panels (a)–(c) and (d)–(f), respectively. Each position represents a specific Wyckoff site. The absorbing atoms are surrounded by circles indicating the emitted photoelectron wave.

ties (e.g., the probabilities that the TM_P or TM_O sites are occupied by Fe). However, on the macroscopic scale one knows the ratio $n_{Fe}:n_{Mn}=x:(2-x)$ of the numbers of Fe and Mn atoms, respectively. With this restriction, all probabilities can be expressed by only one appropriately chosen free parameter. In the present work, the parameter was chosen to coincide with the probability δ to find Fe on the TM_P site. Since this parameter incorporates the distribution of Fe and Mn on the two possible sites, it is the most interesting parameter in the fits of the EXAFS data. From δ, the weighting coefficients of the individual models can be determined and taken into account by the S_0^2 parameter [being $D_j(k,r_j)$ in Eq. (1)] of the ARTEMIS program.

Now we want to consider case (A). The Fe K EXAFS signal will then be a superposition of both, Fe on TM_P and Fe on TM_O site. In case of Mn as the absorbing atom, the situation is exactly the same. Figure 5 schematically visualizes this situation. For the Mn K EXAFS signal the three situations (a)–(c) of Fig. 5 contribute to the signal, the Fe K EXAFS consists of contributions (d)–(f), respectively. Regarding the indistinguishability of Fe and Mn the situations (a) and (e), (b) and (d) as well as (c) and (f) are pairwise equivalent and will provide indistinguishable Fe K and Mn K EXAFS signals. Considering this, one can show that, as a first approximation, there is no difference in the $\chi(k)$ functions (EXAFS signals) corresponding to situations (a) and (e), (b) and (d) or (c) and (f).

Using the probabilities of Fig. 6, the Mn K EXAFS signal can be written in the following form:

$$\chi_{Mn}(k) = p_{MF} \cdot \chi_a(k) + p_{FM} \cdot \chi_b(k) + p_{MM} \cdot \chi_c(k) \qquad (4)$$

and for the Fe K EXAFS signal,

$$\chi_{Fe}(k) = p_{MF} \cdot \chi_d(k) + p_{FM} \cdot \chi_e(k) + p_{FF} \cdot \chi_f(k). \qquad (5)$$

Since situations (a) and (e), (b) and (d), and (c) and (f), respectively, are pairwise equivalent and (a) and (d) as well as (b) and (e) represent the same unit cells, Eq. (5) changes to

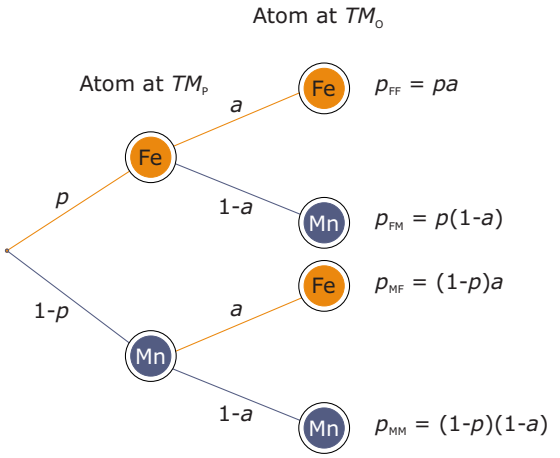

FIG. 6. (Color online) Probabilities p and a for the possible situations (distribution of Mn and Fe on TM_P and TM_O site, respectively) occurring in one unit cell of $YMnFeO_5$.

$$\chi_{Fe}(k) = p_{MF} \cdot \chi_b(k) + p_{FM} \cdot \chi_a(k) + p_{FF} \cdot \chi_c(k). \qquad (6)$$

Finally, we consider the EXAFS signal for the sample with $x=1$ ($YMnFeO_5$). Here p_{MM} and p_{FF} as well as p_{MF} and p_{FM} are the same and we find

$$\chi_{Fe}(k) = p_{MF} \cdot \chi_b(k) + p_{MF} \cdot \chi_a(k) + p_{MM} \cdot \chi_c(k) = \chi_{Mn}(k). \qquad (7)$$

Hence, if the assumption (A) is correct, the Fe K and the Mn K EXAFS signals would be identical for $x=1$. Taking Fig. 3(d) into account we can conclude that case (A) was not observed since both EXAFS curves are significantly different. Thus, assumption (A) will be neglected in the following.

These considerations have shown that Fe and Mn atoms prefer a certain ordering within the unit cell rather than a random distribution. A more quantitative analysis with respect to cases (B), (C), and (D) will be given in the next section. The same equations [Eqs. (4) and (5)] can be used whereas the coefficients for a certain distribution of Mn/Fe atoms can be determined from the parameter δ. Therefore, cases (B) and (C) are characterized by $\delta=0$ and $\delta=1$, respectively, and case (D) by $\delta \in (0,1)$.

B. Quantitative analysis of EXAFS data

At first the assumptions (B) and (C) were tested separately using different models (including cluster sizes) and a certain number of different refined parameters (for instance, lattice parameters, Debye-Waller factors or certain constraints). It turned out that assumption (C), Fe on position TM_P, gave always much better fit qualities independent of the amount of refined parameters N_p. The R values are half the values of assumption (B) as can be seen in Table IV. Due to the low R values of about a few percent it can be expected, that Mn and Fe are distributed accordingly.

After this rather simple approach much more complex models were tested: a total of approximately 100 single and

TABLE IV. Quality parameters (R values) with respect to the number of free parameters N_p refined against experimental data of sample $YMnFeO_5$. The structure models were tested separately with respect to assumptions (B) and (C). It can be seen that assumption (C), at which Fe is located on position TM_P, gave always much better fit qualities.

	Fe K EXAFS		Mn K EXAFS	
N_p	$R_{(B)}$	$R_{(C)}$	$R_{(B)}$	$R_{(C)}$
3	0.266	0.108	0.495	0.187
5	0.212	0.087	0.369	0.085
8	0.148	0.053	0.233	0.079
10	0.174	0.055	0.352	0.068
13	0.159	0.052	0.156	0.072

approximately 100 multiple-scattering paths generated from clusters with radii of about 6.5 Å were considered. The best fits to the data can be found in Fig. 7. The corresponding refined parameters are listed in Table V.

The fits are in rather good agreement with the experimental data, for the Mn K EXAFS as well as for the Fe K EXAFS data, although no structural parameters were refined. Even though the distribution parameter δ was refined [assumption (D)] for every data set (see Table V), its value resulted in unity with respect to the estimated standard deviations esd (these values are given in brackets in Table V) supporting model (C). It can be seen that the fits of the Fe K EXAFS provided much more reliable results (lower values of R and esd). This is attributed to the increased number of data points (see Sec. II B) providing a better data-to-parameter ratio. In Fig. 7(b), the interpolation of the experimental data of samples with $x=0$ and $x=1$ $[1/2\cdot\chi_{YMn_2O_5}(k)+1/2\cdot\chi_{YMnFeO_5}(k)]$ as well as the residual between both curves are shown. An excellent agreement can be noticed, which suggests a linear behavior of the structural changes with increasing the Fe content.

Since in Ref. 32 a shifting of the TM_P site toward the apex of the pyramid was observed with increasing Fe content, the idea arose that a site splitting might exists for low Fe concentrations, e.g., two different atomic environments (one for Mn at TM_P and the other for Fe at TM_P) rather than a mean environment. We tried to address this assumption using additional refinements. No lower R values were obtained, instead, nonphysical atomic coordinates due to parameter correlation effects and, at the same time, too large esd restricted the reliability.

We also tried to inspect the influence of an additional crystallographic phase content observed in Ref. 32, i.e., Fe_2O_3. Taking the additional phases into account, no significant improvements of the fits were observed and very large esd of the parameters were obtained. Hence, it was not possible to observe an influence of such additional phases on the EXAFS signal, probably due to the small contributions of these phases.

In conclusion, based on EXAFS analysis we have shown that Fe favors the TM_P site. This is not unexpected since the formal average charge of this position is determined to be +3 (+4 for the TM_O site) and the Fe atom itself favors the oxi-

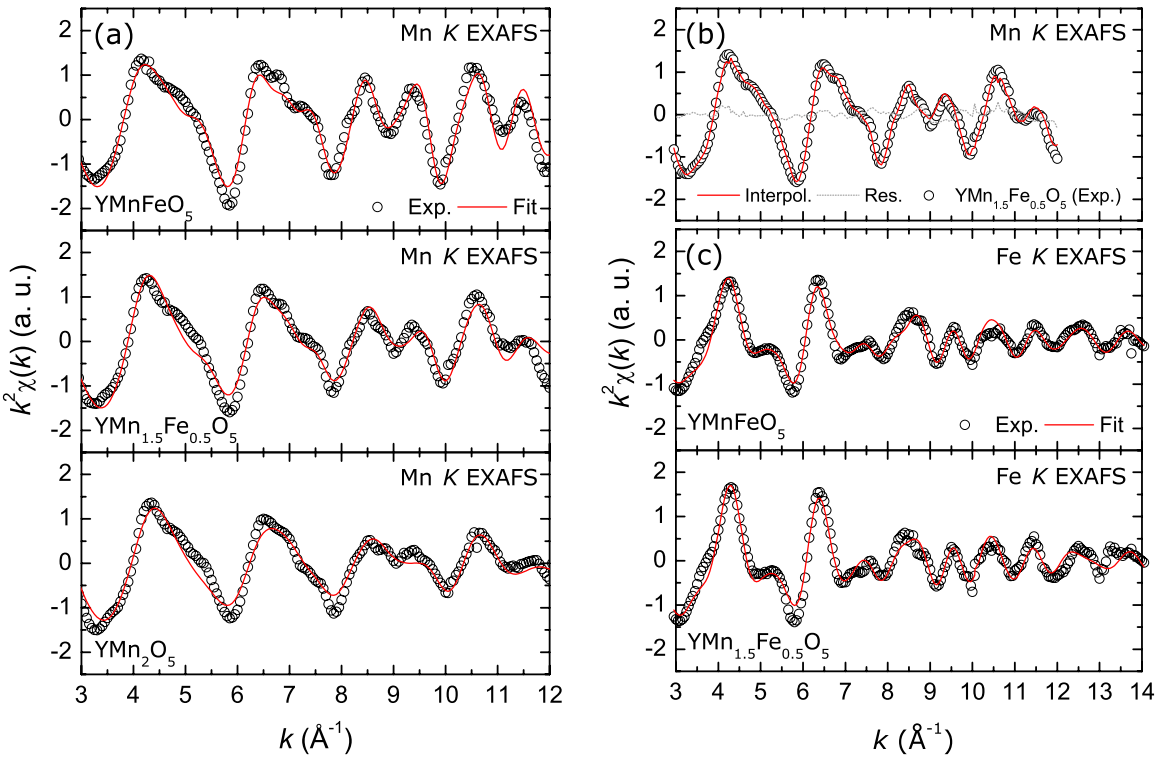

FIG. 7. (Color online) The refined EXAFS functions $\chi(k)$ for (a) the Mn K EXAFS and (c) the Fe K EXAFS are shown. Note, in (b) the experimental data of the Mn K EXAFS ($YMn_{1.5}Fe_{0.5}O_5$) are depicted together with an interpolation of the experimental data of both other samples $[1/2\cdot\chi_{YMn_2O_5}(k)+1/2\cdot\chi_{YMnFeO_5}(k)]$ as well as the residual between both curves (light-gray line).

TABLE V. Refined parameters of the best fits according to assumption (D) are summarized: the proportion of Fe on the TM_P site δ and thermal displacement parameters of the Y, *TM*, and O atoms σ^2_Y, σ^2_{TM}, and σ^2_O. The structure parameters were kept fixed during refinements (see Ref. 32). Note that $\delta=1$ refers to a maximal occupancy of the TM_P site by Fe atoms with respect to the content *x*.

	YMn_2O_5	$YMn_{1.5}Fe_{0.5}O_5$		$YMnFeO_5$	
Parameter	Mn *K*	Fe *K*	Mn *K*	Fe *K*	Mn *K*
R	0.0815	0.0164	0.0129	0.0193	0.0352
δ		1.00(6)	0.99(32)	1.00(3)	0.99(13)
σ^2_Y (Å^2)	0.001(5)	0.001(1)	0.001(3)	0.004(2)	0.002(2)
σ^2_{TM} (Å^2)	0.001(3)	0.002(1)	0.001(1)	0.001(1)	0.001(1)
σ^2_O (Å^2)	0.002(2)	0.004(1)	0.001(1)	0.003(1)	0.001(1)
Cluster radius (Å)	6.5	6.0	6.5	6.5	6.5

dation states +2 and +3. Mn on the other hand favors the oxidation states +2, +4, +6, and +7 (Ref. 39) so that the Mn atom prefers the TM_O site.

Specific results of the EXAFS analysis are: (i) assumption (A), that Fe and Mn are distributed randomly, is unlikely because otherwise the Fe *K* and the Mn *K* EXAFS would be nearly equal for the $x=1$ sample and this is not the case, (ii) assumption (B), that Fe is located completely on position TM_O and Mn on TM_P, resulted in large *R* values, even with a large number of free parameters, and can therefore be excluded, (iii) assumption (C), that Fe is located completely on position TM_P and Mn on TM_O, is the most favorable result, since also (iv) assumption (D), that Fe is inhomogeneously distributed over both sites, is pointing at a maximal occupancy of the TM_P site by Fe atoms (best fit qualities and δ is equal to unity).

Since the Fe *K* absorption edge is only 570 eV above the Mn *K* edge, the EXAFS oscillations corresponding to the Mn *K* edge are still present in the Fe EXAFS data. Therefore, the data points beyond the Fe *K* absorption edge can be attributed either to photoelectrons from Fe or Mn atoms with different kinetic energy and thus different *k* values. So, Fe EXAFS oscillations are superposed by oscillations corresponding to the Mn EXAFS with a higher *k* value. For large *k*, the $\chi(k)$ signal is modulated by a power function $y=ck^b$ with *c* being a constant and $b\approx-3.3$, which is due to the asymptotic behavior of the reflection amplitudes according to McKale *et al.*[46] and the overall factor of $1/k$ on the EXAFS function [Eq. (1)]. Using such a function to approximate the $\chi_{Mn}(k)$ EXAFS function in the region of $\chi_{Fe}(k)$, one can reasonably estimate the amount of perturbation in the Fe EXAFS due to this effect. For $k=2$ Å^{-1} in the Fe EXAFS, this gives an amount of approximately 1% but for $k=14$ Å^{-1} the perturbation is in the order of approximately 28% of the Fe EXAFS signal. This one has to keep in mind concerning the accuracy of EXAFS results. Also, this could explain minor differences between experimental data and corresponding simulations for the Fe EXAFS at high-*k* values.

C. XANES interpretation

As we found a significant shift of the Mn *K* absorption edge energy [see Fig. 4(a)] to higher energies with increasing amount of Fe within the crystal structure, we now want to give a theoretical basis for this observation.

Considering the occupancy of the different *TM* sites we calculated two different XANES spectra: (i) for the octahedrally and (ii) for the pyramidally coordinated *TM* atom, respectively. In case of the YMn_2O_5 and the $YMnFeO_5$, the data of both environments with the particular *TM* were merged. These spectra are shown in Fig. 8(b). To account for a constant energy shift, which is known to be inherent to the theoretical data calculated by the FEFF program, the energy scale was shifted by −5.54 eV with respect to the experimental spectrum of YMn_2O_5 so that both spectra are congruent. Since the FEFF program is not able to calculate core-level

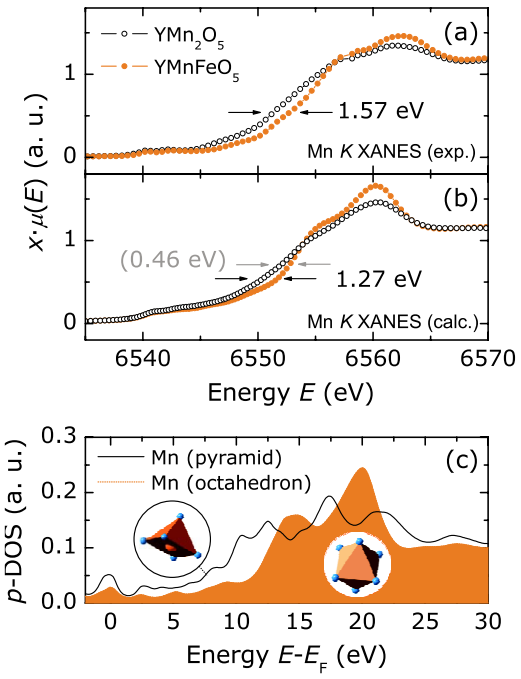

FIG. 8. (Color online) In (a) the experimental XANES spectra of the Mn *K* edge of sample YMn_2O_5 and $YMnFeO_5$ are replotted for comparison purposes. The theoretical XANES spectra, calculated on the basis of structure data given in Ref. 32 and using program FEFF 8.2, are shown in (b). Significant contributions to the XANES spectra in the edge region can be attributed to the DOS of the *p* states of the *TM* atoms (c).

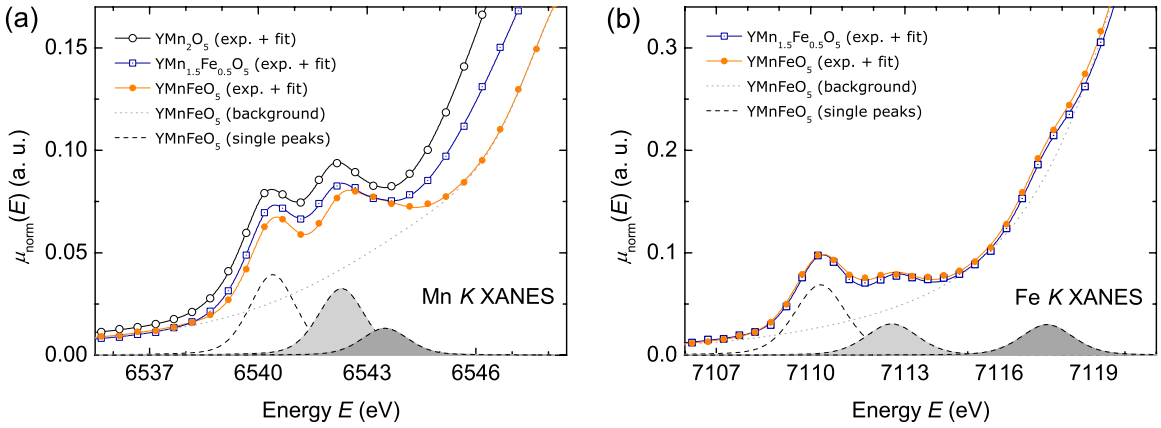

FIG. 9. (Color online) Fits of Mn *K* (left) and Fe *K* (right) pre-edge regions of XAS data using three Pseudo-Voigt peak functions. Fitting results for Mn are given in Table VI.

shifts in the initial state, the Fermi levels (corresponding to the threshold for transitions) should be at the same energy in the calculated spectra, another shift of 0.38 eV was applied to the calculated Mn *K* XANES with Mn on the TM_P site. This is exactly the difference of the muffin-tin potential zero energies and the Fermi-level energies of the calculated spectra.

Comparing the theoretical spectra [Fig. 8(b)] with the experimental ones [Fig. 8(a)], an excellent agreement can be found including the shifting of the Mn *K* absorption edge energy to higher values and the enhancement of the white-line region upon increasing the Fe content. We have to note that the values for the absorption edge energies calculated by the first derivative yielded a rather small energy difference of 0.46 eV. Nevertheless, the maximum energy difference between both spectra is 1.27 eV [marked in Fig. 8(b)] which is close to the experimental value. An estimation of δ, taking the energy shift and its esd into account, yields $\delta \geq 0.96$. We therefore assume that the Fe atoms occupy exclusively the TM_P site, thereby confirming the EXAFS results. Similar shifts of the *TM K* absorption edge in dependence on the *TM* concentration have also been observed by, e.g., Sikora *et al.*[47] on $LaMn_{1-x}Co_xO_3$ and Haas *et al.*[48] on $LiFePO_4$.

Due to the selection rules for transitions induced by photon scattering, the absorption increase at a *K* edge is mainly caused by electronic transitions from core 1*s* states of the absorbing atom to its unoccupied *p* states, in particular, the 4*p* states of Mn and Fe, respectively. The latter states are nonlocal, spatially distributed states. In case of the oxides discussed, the density of states (DOS) for the final states in the first 10 eV above the Fermi level, the pre-edge region of the recorded XANES spectra, is comparatively low [Fig. 8(c)]. Thus, we conclude from the experiments that those states should differ in energy. Since they are widely extended in space, this energy difference is likely to be related to the Coulomb repulsion from the surrounding oxygen atoms. In that case, the Mn on the TM_O site will experience stronger repulsion by its six oxygen neighbors than the TM_P site with five neighbors. This can explain the observed shift of the Mn absorption edge to higher energies, in case only the octahedrally coordinated site TM_O is occupied by Mn atoms.

Regarding the pre-edge region of the XAS data, valuable information can be extracted from fitting the occurring pre-edge features. Therefore, we followed the method described in Refs. 49 and 50 and used three Pseudo-Voigt functions (plus a background function consisting of two additional Pseudo-Voigt functions) to describe the Mn and Fe pre-edge regions. Width and Gauss-Lorentz ratio were constrained to a common value for all pre-edge peaks whereas areas and energy positions were independent. Fitting results are exemplified in Fig. 9. Comparison of the Mn centroid positions with data from Ref. 51 provides oxidation numbers that agree well with the nominal values computed from the composition of the respective compounds (see Table VI).

Furthermore, the total area of the pre-edge peaks is a measure of the symmetry of the coordination polyhedra surrounding the scattering Fe and Mn atoms, respectively. Lower intensity, i.e., area, relates to higher symmetry and vice versa. Thus, the computed Mn total area values (see Table VI) give an increasing symmetry in the sequence of increasing Mn valence. This is in excellent agreement with the respective structures determined in Ref. 32.

No significant change is observed for centroid [$\Delta E = 0.00(7)$ eV] and total area of the Fe pre-edge features [see Fig. 9(b)]. Again, this is in agreement with the presented structure solutions because Fe coordination and oxidation state remain unchanged in the investigated compounds.

Summarizing the XANES analysis, we could clearly show that the differences within the Mn *K* XANES spectra in dependence on *x* can be attributed to the different environment of the *TM* atoms. This is due to the change in their individual contributions to the average XANES signal, i.e., by lowering the Mn occupancy at the TM_P site with increasing the Fe content *x*. For $x=1$, a maximal occupancy of the TM_P site by Fe atoms was obtained. Furthermore, an increasing oxidation number of Mn from +3.5 to +4 as well as an unchanged oxidation state of Fe was determined.

D. DFT interpretation

As shown by the experiments and evaluated by DFT calculations (Sec. II D) Fe favors the TM_P site in the $YFeMnO_5$ structure and prefers a formal oxidation state of +3, whereas the TM_O position is predominantly occupied by Mn^{4+}. The large energy difference between a "disordered" Mn-Fe dis-

TABLE VI. Fitting results for Mn *K* pre-edge region using the method from Ref. 50 (standard deviations given in parentheses). Mn valence after Ref. 51 were extracted using E_c.

	YMn_2O_5	$YMn_{1.5}Fe_{0.5}O_5$	$YMnFeO_5$
Nominal Mn ox. number	$+3\frac{1}{2}$	$+3\frac{2}{3}$	+4
Peak position E_1 (eV)	6540.23(3)	6540.33(2)	6540.40(2)
Peak position E_2 (eV)	6542.08(8)	6542.16(5)	6542.29(4)
Peak position E_3 (eV)	6543.10(30)	6543.30(13)	6543.49(11)
Centroid position E_c (eV)	6541.32(8)	6541.41(4)	6541.60(4)
Valency after Ref. 51	3.4–3.6	3.6–3.7	4.0–4.1
Peak area A_1	0.056(11)	0.050(4)	0.039(3)
Peak area A_2	0.051(10)	0.042(4)	0.033(6)
Peak area A_3	0.012(6)	0.012(2)	0.013(4)
Total area A_t	0.119(27)	0.103(10)	0.085(13)

tribution and the more stable "ordered" Mn-Fe one ($\Delta E = 1$ eV) allows for only a small amount of such disorder. An analysis of the density of electronic states helps to elucidate the electronic origin of this preference.

FPLO-7 supports the calculation of site and angular momentum (l and m) resolved DOS by projection onto real-space spherical harmonics. An orthogonal coordinate system (x,y,z) centered at the projection site is chosen such that the z axis is aligned with the high-symmetry line to the apex atom(s) of the *TM* coordination polyhedra, and the x and y directions are aligned to high-symmetry directions in the plane perpendicular to z. As the cluster calculation does not make use of periodic boundary conditions the DOS shows the pure crystal-field splitting of the metal $3d$ orbitals without dispersion. In the corresponding figures (see below), the orbital energy levels are broadened by applying a Fermi broadening with an electron temperature of 100 K.

As discussed above (Table III), the TM_P (Fe^{3+}) position differs from TM_P (Mn^{3+}) while TM^{4+} is always centrally located inside the octahedron. A crystal-field consideration can explain this finding for the pyramid: for both ions the exchange splitting dominates the crystal-field splitting. In high-spin Mn^{3+} only four local d orbitals are occupied. The $d_{x^2-y^2}$ orbital, which most strongly interacts with the oxygen neighbors of the basal plane, is unoccupied here. Hence, the position close to the basal plane is more favorable for Mn^{3+}. In contrast, for the Fe^{3+} ion all d orbitals are occupied with one electron each. Under this condition, the repulsive interactions between the singly occupied Fe d levels and the negatively charged O sites are reduced if Fe is shifted away from the basal plane toward the center of the pyramid. There, four of the five oxygen neighbors are nearly equidistant and only one unfavorably short *TM*-O bond occurs. In the case of the Fe atom, the energy gained by this displacement (calculated from the total-energy difference for both positions) amounts to 0.14 eV. When the local DOS of Fe at the pyramid site is closely inspected [see Fig. 10(a)] a rather strong splitting of the orbital energies can be noticed, however, not strong enough to enforce a low-spin configuration. The highest occupied orbital in this case is the $d_{x^2-y^2}$ orbital (unoccupied for Mn^{3+}).

For the weakly distorted octahedron, the calculated orbital energies closely follow the crystal-field splitting of an ideal cubic case: five $3d$ orbitals form two nearly degenerate sets of three (t_{2g} containing d_{xy}, d_{xz}, and d_{yz}) and two (e_g containing d_{z^2} and $d_{x^2-y^2}$) orbitals. This is clearly revealed by the corresponding local DOS curves [compare Figs. 10(a) and 10(b) for the Fe atoms]. Mn^{4+} with d^3 occupation fits well into this environment by occupying only the low-lying t_{2g} states in a spin-polarized manner. For Fe^{4+} two possible electronic configurations exist. In a high-spin configuration, the t_{2g} orbitals are singly occupied and the remaining electron is shared among the e_g orbitals. In the low-spin case, preferred here, the e_g manifold is empty and four electrons are distributed in the three t_{2g} orbitals. In the local DOS for the low-spin case [Fig. 10(b)], this causes the Fermi level to pass through the t_{2g} orbitals. This situation would in general cause a Jahn-Teller distortion of the environment resulting in a reduction in symmetry. This means that the experimentally observed polyhedron would not be stable against distortion if Fe^{4+} were located in the center. Hence, both the crystal-field energy (high-spin case) and the intra-atomic exchange interaction (low-spin case) prevent the incorporation of Fe^{4+} within the octahedron. Thus, the present crystal-field analysis yields a clear preference for Mn^{4+} at the octahedral site and Fe^{3+} at the pyramidally coordinated site.

V. CONCLUSION

The Mn, Fe, and Y local structures in the multivalence $YMn_{2-x}Fe_xO_5$ series are investigated by x-ray absorption spectroscopy, i.e., EXAFS and XANES, respectively. A site selective substitution behavior with the non-Jahn-Teller ion Fe^{3+}, conserving the orthorhombic space-group symmetry, is verified. The systematic evolution of EXAFS spectra with x is observed only for the Mn K absorption edge. For the Y K as well as for the Fe K edge, no significant differences and rather equal spectra are found. The same observations as for the EXAFS spectra are made for the XANES spectra.

We can clearly identify the Wyckoff site $4h$ (TM_P) as the site at which the Fe atoms with oxidation number +3 are incorporated. This is possible since two different electronic environments for the *TM* atoms exist in the unit cell. As a result, $(100 \pm 3)\%$ of the Fe atoms occupy the pyramidally coordinated *TM* site in case of the sample with $x=1$. For

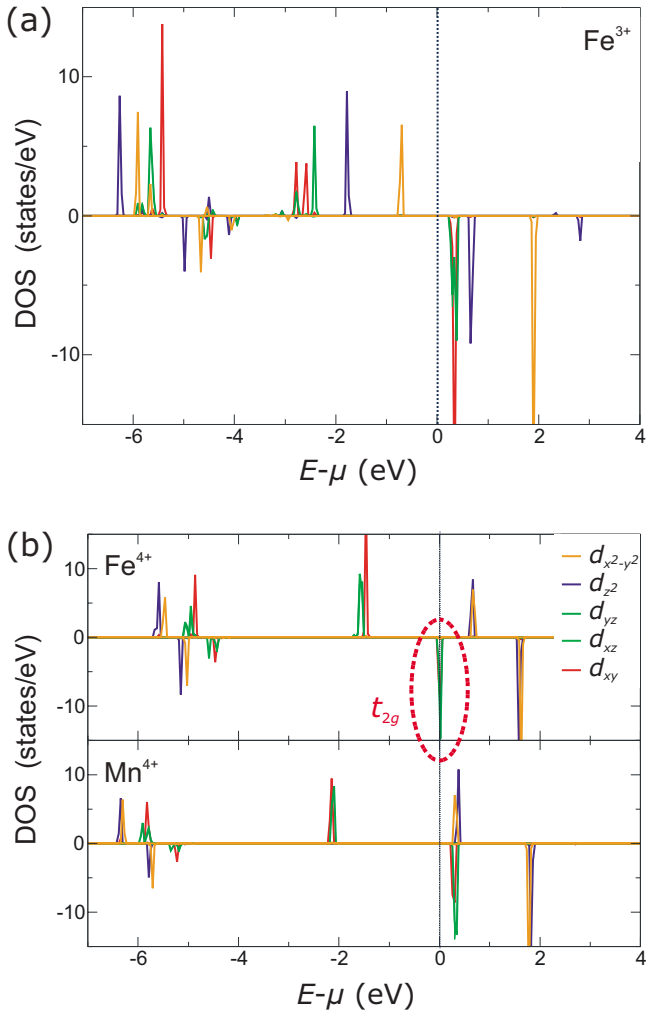

FIG. 10. (Color online) Local DOS calculated for (a) the Fe^{3+} ion inside the pyramid and (b) the Fe^{4+} and Mn^{4+} ion inside the octahedron, respectively. The atomic coordinates of Fe [in (a)] were taken from the DFT calculations whereas for the other one they were adopted from the experimentally determined structure data of $YFeMnO_5$ (Ref. 32). μ is the chemical potential which at 0 K corresponds to the Fermi level. A strong splitting of the orbital energies of the Fe^{3+} ion inside the pyramidal environment can be seen (a). If a Fe^{4+} ion would be incorporated within an octahedron this would result in a Jahn-Teller distortion not observed by the experiments.

lower Fe content ($x=0.5$), it could be shown that $(100\pm6)\%$ of the Fe atoms available are located at the pyramidally coordinated *TM* site. Thus, we suggest a linear behavior of the Fe content x and the occupation of the TM_P site by Fe atoms (instead of Mn) verified by a dedicated interpolation. Congruent with the oxidation state of the Fe atoms an increase in the oxidation number of the Mn ions with growing x is determined quantitatively.

In accordance with the selection rules for dipole transitions, the contributions to the change in the XANES spectra are attributed to the *TM* $1s$-$4p$ transitions. Multipole transitions were tested but their contributions to the Mn *K* XANES are not significant so that these transitions turned out to be unlikely.

From our investigations, site disorder, as it is reported by Muñoz *et al.*[29] and de la Calle *et al.*,[27] seems to be very unlikely for our samples. Nevertheless, a 3% disorder of Mn/Fe atoms for the composition $x=1$ cannot be excluded taking our esd into account.

The DFT calculations presented justify the assignment of the *TM* ion with +4 oxidation state to the octahedral and the *TM* ion with +3 oxidation state to the pyramidal environment. From the local DOS of the *TM* ions inside the octahedron a nearly undistorted cubic crystal-field splitting of the $3d$ states is found. Because Mn^{4+} with its three localized $3d$ electrons fits well with the threefold degenerate t_{2g} states of the cubic crystal field, Fe is favorably incorporated within the pyramidal environment.

The experimentally observed distortion of the pyramid due to Fe incorporation is attributed to crystal field rather than specific Jahn-Teller effects. Concerning the octahedron a Jahn-Teller-type distortion is also excluded since Mn^{4+} exhibits an unoccupied $d_{x^2-y^2}$ orbital. Hence, a distortion of the octahedron is not favored by this type of ion. Therefore, the present distortions are attributed to the complex crystal structure and secondary-order effects. In summary, the structural complexity observed for the $YMn_{2-x}Fe_xO_5$ system cannot be attributed to the presence of Jahn-Teller distortions. Instead, one has to take the magnitude of the individual contributions of all the interactions into account.

ACKNOWLEDGMENTS

This research was in part carried out at the light source facilities DORIS III at HASYLAB/DESY. DESY is a member of the Helmholtz Association (HGF). We would like to thank D. Novikov and K. Rickers for assistance in using beamline C1 (CEMO). Moreover, we thank the Deutsche Forschungsgemeinschaft (DFG) for financial support within the Sonderforschungsbereich (SFB) 463 as well as the BMBF for funding via the "Pakt für Forschung und Innovation." A.L. acknowledges financial support within the European Union under the Framework 6 program under a contract for an Integrated Infrastructure Initiative (Reference No. 026019 ESTEEM).

[1] N. Setter, D. Damjanovic, L. Eng, and G. Fox, J. Appl. Phys. **100**, 051606 (2006).
[2] N. A. Hill, J. Phys. Chem. B **104**, 6694 (2000).
[3] T. Kimura, S. Kawamoto, I. Yamada, M. Azuma, M. Takano, and Y. Tokura, Phys. Rev. B **67**, 180401(R) (2003).
[4] L. Fuentes, M. García, J. Matutes-Aquino, and D. Ríos-Jara, J. Alloys Compd. **369**, 10 (2004).
[5] A. Sharan, J. Lettieri, Y. F. Jia, W. Tian, X. Q. Pan, D. G.

Schlom, and V. Gopalan, Phys. Rev. B **69**, 214109 (2004).
[6] S. Picozzi and C. Ederer, J. Phys.: Condens. Matter **21**, 303201 (2009).
[7] A. Loidl, H. von Löhneysen, and G. M. Kalvius, J. Phys.: Condens. Matter **20**, 430301 (2008).
[8] K. Dörr and C. Thiele, Phys. Status Solidi B **243**, 21 (2006).
[9] *Physics of Ferroelectrics: A Modern Perspective*, Topics in Applied Physics Vol. 105, edited by K. Rabe, C. H. Ahn, and J.-M. Triscone (Springer, Berlin, 2007).
[10] S. Gemming, W. Alsheimer, R. Luschtinetz, G. Seifert, C. Loppacher, and L. M. Eng, J. Comput.-Aided Mater. Des. **14**, 211 (2007).
[11] A. Rother *et al.*, Phys. Rev. B **74**, 134116 (2006).
[12] T. Leisegang, H. Stöcker, A. A. Levin, T. W. Weißbach, M. Zschornak, E. Gutmann, K. Rickers, S. Gemming, and D. C. Meyer, Phys. Rev. Lett. **102**, 087601 (2009).
[13] G. Suchaneck, V. S. Vidyarthi, G. Gerlach, M. Reibold, A. A. Levin, and D. C. Meyer, Ferroelectrics **370**, 104 (2008).
[14] A. Ikeda and K. Kohn, Ferroelectrics **169**, 77 (1995).
[15] A. Inomata and K. Kohn, J. Phys.: Condens. Matter **8**, 2673 (1996).
[16] J. A. Alonso, M. T. Casais, M. J. Martínez-Lope, J. L. Martínez, and M. T. Fernández-Díaz, J. Phys.: Condens. Matter **9**, 8515 (1997).
[17] N. Hur, S. Park, P. A. Sharma, J. S. Ahn, S. Guha, and S.-W. Cheong, Nature (London) **429**, 392 (2004).
[18] C. R. dela Cruz, F. Yen, B. Lorenz, M. M. Gospodinov, C. W. Chu, W. Ratcliff, J. W. Lynn, S. Park, and S.-W. Cheong, Phys. Rev. B **73**, 100406(R) (2006).
[19] S.-W. Cheong and M. Mostovoy, Nature Mater. **6**, 13 (2007).
[20] R. Feyerherm, E. Dudzik, A. U. B. Wolter, S. Valencia, O. Prokhnenko, A. Maljuk, S. Landsgesell, N. Aliouane, L. Bouchenoire, S. Brown, and D. N. Argyriou, Phys. Rev. B **79**, 134426 (2009).
[21] C. Y. Ren, Phys. Rev. B **79**, 125113 (2009).
[22] H. Kimura, Y. Noda, and K. Kohn, J. Magn. Magn. Mater. **321**, 854 (2009).
[23] K. Kohn, Ferroelectrics **162**, 1 (1994).
[24] A. Muñoz, J. A. Alonso, M. J. Martínez-Lope, and J. L. Martínez, Phys. Rev. B **72**, 184402 (2005).
[25] A. Muñoz, J. A. Alonso, M. J. Martínez-Lope, and J. L. Martínez, Eur. J. Inorg. Chem. **2007**, 1972 (2007).
[26] E. F. Bertaut, G. Buisson, A. Durif, J. Mareschal, M. C. Montmory, and S. Quezel-Ambrunaz, Bull. Soc. Chim. Fr. **65**, 1132 (1965).
[27] C. de la Calle, J. A. Alonso, M. J. Martínez-Lope, M. García-Hernandez, and G. Andre, Mater. Res. Bull. **43**, 97 (2008).
[28] T.-C. Han and J. G. Lin, J. Appl. Phys. **99**, 08J508 (2006).
[29] A. Muñoz, J. A. Alonso, M. J. Martínez-Lope, and J. L. Martínez, Chem. Mater. **16**, 4087 (2004).
[30] J. B. Goodenough, Annu. Rev. Mater. Sci. **28**, 1 (1998).
[31] R. G. Burns, *Mineralogical Applications of Crystal Field Theory*, 2nd ed. (Cambridge University Press, Cambridge, 1993).
[32] T. Leisegang, T. Führlich, T. Weißbach, F. Wunderlich, D. Souptel, and D. C. Meyer, J. Alloys Compd. (to be published).
[33] D. Souptel, *Crystal growth and properties of novel multiferroic oxide compounds.*, Project SO840/1-1 (2007).
[34] K. V. Klementiev, XAFSMASS., freeware: www.desy.de/~klmn/xafsmass.html (2003).
[35] P. A. Lee, P. H. Citrin, P. Eisenberger, and B. M. Kincaid, Rev. Mod. Phys. **53**, 769 (1981).
[36] S. I. Zabinsky, J. J. Rehr, A. Ankudinov, R. C. Albers, and M. J. Eller, Phys. Rev. B **52**, 2995 (1995).
[37] K. Rickers, U. Brüggmann, W. Drube, M. Herrmann, J. Heuer, E. Welter, H. Schulte-Schrepping, and H. Schulz-Ritter, in *Proceedings of the Ninth International Conference on Synchrotron Radiation Instrumentation*, AIP Conf. Proc. No. 879, edited by J.-Y. Choi and S. Rah (AIP, New York, 2007), pp. 907–910.
[38] K. Rickers, W. Drube, H. Schulte-Schrepping, E. Welter, U. Brüggmann, M. Herrmann, J. Heuer, and H. Schulz-Ritter, in *X-Ray Absorption Fine Structure XAFS13: 13th International Conference on X-Ray Absorption Fine Structure*, AIP Conf. Proc. No. 882, edited by B. Hedman and P. Pianetta (AIP, New York, 2007), pp. 905–907.
[39] B. Ravel and M. Newville, J. Synchrotron Radiat. **12**, 537 (2005).
[40] A. L. Ankudinov, C. E. Bouldin, J. J. Rehr, J. Sims, and H. Hung, Phys. Rev. B **65**, 104107 (2002).
[41] L. Hedin and B. I. Lundqvist, J. Phys. C **4**, 2064 (1971).
[42] A. L. Ankudinov and J. J. Rehr, Phys. Rev. B **62**, 2437 (2000).
[43] M. S. Moreno, K. Jorissen, and J. J. Rehr, Micron **38**, 1 (2007).
[44] K. Koepernik and H. Eschrig, Phys. Rev. B **59**, 1743 (1999).
[45] J. P. Perdew and Y. Wang, Phys. Rev. B **45**, 13244 (1992).
[46] A. G. McKale, B. W. Veal, A. P. Paulikas, S. K. Chan, and S. Knapp, J. Am. Chem. Soc. **110**, 3763 (1988).
[47] M. Sikora, C. Kapusta, K. Knizek, Z. Jirak, C. Autret, M. Borowiec, C. J. Oates, V. Prochazka, D. Rybicki, and D. Zajac, Phys. Rev. B **73**, 094426 (2006).
[48] O. Haas, A. Deb, E. J. Cairns, and A. Wokaun, J. Electrochem. Soc. **152**, A191 (2005).
[49] M. Wilke, F. Farges, P. E. Petit, G. E. Brown, and F. Martin, Am. Mineral. **86**, 714 (2001).
[50] F. Farges, Phys. Rev. B **71**, 155109 (2005).
[51] E. Chalmin, F. Farges, and G. E. Brown, Contrib. Mineral. Petrol. **157**, 111 (2009).